Physica 19D (1986) 334–354
North-Holland, Amsterdam

REDOX FRONT PROPAGATION AND BANDING MODALITIES*

P. ORTOLEVA, G. AUCHMUTY, J. CHADAM, J. HETTMER, E. MERINO, C.H. MOORE and E. RIPLEY
Geo-Chem Research Associates, Inc., 400 E. Third Street, Bloomington, IN 47401, USA

Received 9 November 1983
Revised 15 September 1985

Oxygenated waters flowing through a reduced sandstone cause propagating redox fronts. Mathematical reaction–transport models of these fronts studied here show a number of nonlinear phenomena including one-parameter families of constant-velocity fronts, decelerating fronts and two types of front instabilities leading to pattern formation. These redox front phenomena are examples of nonlinear wave propagation and self-organization. Redox fronts in nature are economically important because they can trap accumulations of metallic ores. Furthermore, they are but one example of a wider class of water–rock interaction systems rich in nonlinear reaction–transport phenomena.

Analytical results are presented on conservation law and free boundary methods to study the velocity and profiles of the waves. A new model of the Ostwald supersaturation–nucleation–depletion cycle is presented that incorporates features of Liesegang banding not predicted by other formulations: these include finite band widths and continuous undulatory as well as discrete banding.

1. Introduction

Chemical waves have been extensively studied in recent years and a variety of interesting phenomena have been discovered [1–5]. In these studies waves are driven by system-wide, sustained nonequilibrium conditions. Yet another type of driving force for wave propagation exists – an influx of waters that react with a porous medium through which they flow. Our purpose here is to demonstrate that this situation can lead to a variety of nonlinear wave and pattern phenomena.

A common geological example of this type is a so-called redox roll front depicted in fig. 1. In this case water of a given composition flows through a porous rock and reacts with it. As the water advances it eventually becomes equilibrated with the rock. At any given time a moving transition zone exists where the altered rock upstream grades into the unaltered rock downstream. The altered zone may be termed the water–dominated zone since the only minerals that can exist there are those in equilibrium with the inlet waters. On the other hand the unaltered (downstream) zone may be considered the rock dominated zone since the waters there are transformed to a composition in equilibrium with the original rock minerals after passing through the reaction front. We find that in this transition zone the nonequilibrium conditions can permit instability and the development of patterns of deposition. This is expected on quite general grounds from the work of Prigogine and coworkers [6] who find that instability and pattern formation in reaction-transport systems are expressed only under non-equilibrium conditions.

Where meteoric, oxygen-saturated water flows through a porous sandstone that contains pyrite grains (fig. 1), the transition zone is called a redox front [7–9]. The oxygen is consumed in oxidizing the pyrite. The redox front at any given time separates the zone upflow where the pyrite is

*Research supported by a grant from U.S.D.O.E., Office of Basic Energy Sciences, Engineering Research program, Contract #DE-AC02-82 ER12074.

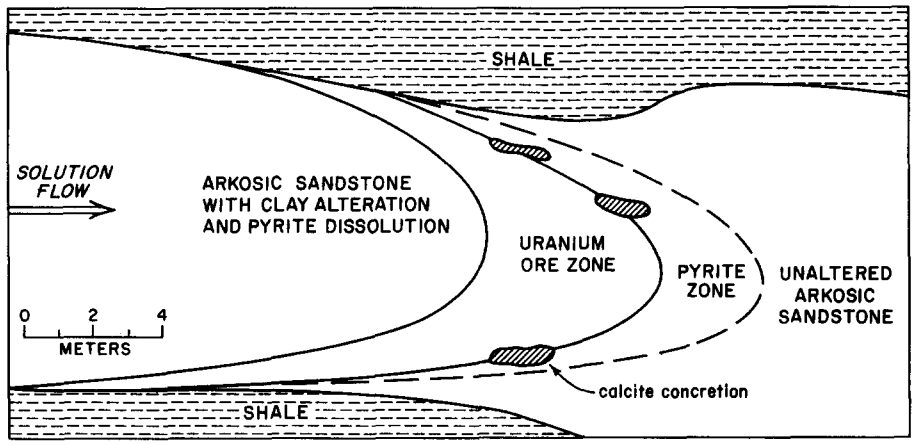

Fig. 1. Idealized cross-section through uranium ore roll front, based on refs. 7 and 9.

oxidatively dissolved out from the zone downflow where it is still at its original level. As the water continues to flow, the redox front advances downflow. Since many useful metal ions (such as copper, molybdenum, selenium, and uranium) form mobile species under oxidizing conditions but relatively insoluble minerals in reducing environments, these redox fronts can act as traps for these metals as low concentration levels in the original rock are accumulated at the interface. The greater the amount of metals trapped the more slowly the front migrates downflow. These accumulations, called roll front deposits, are reviewed in refs. 7–9. The reducing environment in the unaltered rock is due mainly to pyrite and in some cases carbonaceous material (i.e. plant debris in a sandstone).

In the present study several simple models, suggested by these geological redox fronts, are set forth and analyzed to demonstrate the striking variety of nonlinear wave phenomena that these systems may support. We find that while some systems yield stable steady state front advancement, others can rigorously be shown to decelerate continuously as precipitation of one of the minerals at the front takes place. We also find that some systems yield mineral banding while others may sustain a one-parameter family of fronts with strong selection rules – choosing from among the family a single physically realizable one. In other systems a discrete multiplicity of fronts or even temporally oscillatory or chaotic fronts are possible.

All the models discussed here include diffusion of aqueous species, water flow, and dissolution, nucleation, and growth of mineral grains. One of the striking results obtained is that the propagating redox front may leave in its wake a trail of *banded* iron-oxide precipitate. The banding arises through a dissolution–transport–nucleation–growth feedback, as follows. The oxidation of pyrite (iron disulfide, FeS_2) releases ferrous ions and sulfur-bearing ions. The ferrous ion becomes oxidized to ferric ion. The latter then nucleates as iron oxide, but only if and where the concentration product for iron oxide (hematite or goethite) reaches a given value, Q_n, larger than the equilibrium constant Q. Once iron oxide has nucleated at a given place and time, it grows. If the growth is fast enough, it will, by diffusion, bring the surrounding aqueous solution below the nucleation threshold (though not below saturation), both behind and ahead of the point of growth. Thus, the nucleation threshold, Q_n, may not be reached again until a point far enough downflow where sufficient additional pyrite is oxidized, and enough ferrous ion is released but not consumed by the iron oxide precipitation. At this point a new iron oxide zone nucleates and grows. Later, more bands form

farther downflow by the same supersaturation–nucleation–depletion cycle.

In geology such bands are often called Liesegang bands. The above cycle was invoked by Ostwald [15] to explain their genesis. The model presented here for these bands differs from the original formulation of Prager [16]. Unlike the Prager theory the formulation presented here allows for continuous undulatory variations of iron oxide and not only discrete bands with precipitate free gaps separating them. Also, our formulation can describe the finite width of the precipitate-bands. Our model allows for bifurcation analysis of the transition from steady to undulatory profiles of mineral precipitation.

Patterning in water–rock interaction problems may also take on inherently a two-dimensional character. The banding as described above could give way to spotted patterns, for example. Planar water–rock interaction fronts may also undergo morphological instability via a transition to scalloped or fingered fronts [14]. The underlying feedback arises due to a coupling between flow and the mineral dissolution process: mineral dissolution causes increased permeability which in turn causes augmented flow and, via an increased rate of import of reactive waters, an increased rate of dissolution.

The velocity of a steady water–rock interaction front turns out to be independent of the diffusion coefficients of aqueous species and the detailed form of the reaction rates, while the concentration profiles across the front do depend on them. The advancement velocity of a variety of redox fronts is calculated exactly here by demonstrating the existence of a number of constants of steady wave motion. These conservation conditions are shown to hold even for certain nonplanar fronts.

In many situations of geological interest transport is rate limiting for the progress of the mineral reactions. In this "fast reaction" limit we show how the water–rock interaction front equations can be reduced to a free boundary problem. This reduction is used to calculate wave profiles for a number of simple redox front models.

For almost a century there has been interest in patterns of mineralization (bands, rings, mosaic arrays and orbicules) as manifestations of the interaction of precipitation/dissolution reactions and transport [19, 20]. Recent interest in the self–organizing properties of reaction–diffusion systems [21] has regenerated active work on the description and modeling of such phenomena in geochemical systems (see refs. 18, 21, 22 for a review of phenomena and mathematical modeling efforts). The reaction fronts studied herein manifest much of the wealth of nonlinear phenomena found in other reaction–transport models of recent interest although they show interesting mathematical and physical differences from the latter.

2. Decelerating fronts and roll-type deposits

The imposition of reactive waters on a rock does not necessarily lead to a zone of transformation that moves at constant velocity, even assuming that the flow and the initial rock chemistry are constant. In fact in a conspicuous natural instance – the formation of ore bodies at roll fronts as in fig. 1 – this is not the case. To contrast our later results we first examine a case where constant velocity solutions do not exist.

2.1. *A simple roll front deposition model*

Consider the set of reactions

$$X + A \overset{W_1}{\rightleftarrows} Y, \tag{2.1}$$

$$X + B \overset{W_2}{\leftrightarrows} Z, \tag{2.2}$$

where X, Y and Z are mobile aqueous species and A and B are minerals. The detailed form of the rate laws for the dissolution reactions, W_1 and W_2, will not be needed explicitly for our considerations here.

We now investigate the possible existence of a front of constant velocity u for a one-dimensional

aquifer. For such a steady front the concentrations of all species depend only on the front-fixed coordinate φ. With this, and letting v denote the velocity of the water flowing through the porous rock, the reaction–transport equations for X, Y and Z may be written

$$[D_X X' + (u-v)X - uA - uB]' = 0, \tag{2.3}$$

$$[D_Y Y' + (u-v)Y + uA]' = 0, \tag{2.4}$$

$$[D_Z Z' + (u-v)Z + uB]' = 0. \tag{2.5}$$

Here D_X, D_Y and D_Z are the diffusion coefficients of the indicated species and "$'$" = d/dφ.

The phenomenon of interest involves subjecting a rock of given content of minerals A and B to a given inlet water chemistry. Sufficiently downstream of the interaction zone, reactions (2.1), (2.2) are at equilibrium. To ensure this, we must subject the solutions of (2.3)–(2.5) to the following boundary conditions:

$$A, B \underset{\varphi \to -\infty}{\sim} 0, \quad A \underset{\varphi \to \infty}{\sim} A_0, \quad B \underset{\varphi \to \infty}{\sim} B_0, \tag{2.6}$$

$$X \underset{\varphi \to -\infty}{\sim} X_M, \quad Y, Z \underset{\varphi \to -\infty}{\sim} 0, \tag{2.7}$$

$$Y(\infty) = KX(\infty), \quad Z(\infty) = QX(\infty), \quad X(\infty) \equiv X_\infty. \tag{2.8}$$

Conditions (2.8) imply that downstream of the A, B dissolution front Y and Z are at equilibrium for their respective minerals, K and Q being equilibrium constants. A_0 and B_0 are the values of A and B far ahead of the front and we assume the inlet water has no Y or Z.

2.2. *Non-existence of constant velocity fronts*

Eqs. (2.3)–(2.5) indicate the existence of three constants of the front motion (i.e. the three quantities in brackets). Using the conditions at $|\varphi| \to \infty$ to evaluate these constants we get the following three algebraic equations:

$$(u-v)X_\infty - uA_0 - uB_0 = (u-v)X_M, \tag{2.9}$$

$$(u-v)KX_\infty + uA_0 = 0, \tag{2.10}$$

$$(u-v)QX_\infty + uB_0 = 0. \tag{2.11}$$

This is a system of three equations for the two unknowns X_∞ and u. Clearly (2.9)–(2.11) is an over-determined problem, and hence constant velocity solutions do not exist except for very special choices of parameters. This "degeneracy condition" follows directly by solving (2.10, 2.11) for u/X_∞ and equating the results to find

$$A_0/K = B_0/Q. \tag{2.12}$$

If $K = Q$ then we see that this implies that $A_0 = B_0$. When this condition is attained a balance is struck between the A and B front motion so that the advancement is coordinated and steady.

2.3. *Formation of a roll front type deposit*

What is the evolution of the system when (2.12) is not satisfied? To address this we have carried out some numerical simulations of the model (2.1) (2.2). We assumed the rates of mineral dissolution W_1 and W_2 (moles/rock volume-time) are of the mass-action form in the aqueous species concentrations X, Y, Z (moles/rock volume) and are proportional to the mineral grain surface area. The surface area of the grains of mineral A is proportional to $A^{2/3}$ and similarly for B (see the appendix for further details). With this we write

$$W_1 = kA^{2/3}[KX - Y], \tag{2.13}$$

$$W_2 = qB^{2/3}[QX - Z]. \tag{2.14}$$

With these rate laws we write the reaction–transport equations, for a constant flow of velocity v,

$$\frac{\partial X}{\partial t} = D_X \frac{\partial^2 X}{\partial r^2} - v\frac{\partial X}{\partial r} - W_1 - W_2, \tag{2.15}$$

$$\frac{\partial A}{\partial t} = -W_1, \tag{2.16}$$

and similarly for Y, Z and B. The one-dimensional system was taken to be along the r-axis and the evolution in time t was followed. Numerical simulations of these equations were carried out

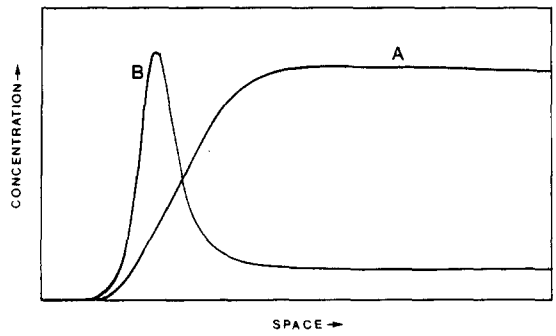

Fig. 2. A, B model of section 2 showing how such a coupled redox system leads to localized deposition (B here) when steady wave non-existence occurs. (This is a schematic summary of numerical solutions of the reaction–transport equations using an approach as outlined in section 6)

using familiar space discretization and iterated backward difference (in time) techniques.

A typical simulation is shown in fig. 2 for parameter values such that $A_0/K \gg B_0/Q$. Under these conditions B is "swept" (by dissolution) and accumulates by reprecipitation as an ever increasing concentration peak at the A redox front. Because the A front has to "sweep" an ever increasing amount of B, the A front moves forward at an ever decreasing speed. A simulation for parameter values such that $A_0/K \ll B_0/Q$ would show a B redox front that traps an ever increasing amount of A. Whichever of the two minerals would by itself generate a faster redox front becomes trapped by the other.

A class of deposits of this type is the so-called uranium roll fronts, in which uranium is trapped by a redox front of pyrite or carbonaceous matter.

The proof of nonexistence does not depend on the detailed form of the rate laws. Rather it follows from the nature of the overall rate process. Conservation conditions as in (2.3)–(2.5) play an important role in analyzing water–rock interaction problems as we now show via other examples. Note however, that while conservation conditions can be used to demonstrate nonexistence, they are not by themselves sufficient to prove the existence of constant-velocity fronts.

3. Exact results for simple redox fronts

A number of exact results can be obtained for simple redox transition front models. These results provide insights into more general processes and are an important check on analytical and numerical techniques developed to handle more complex fronts. Most interesting from the point of view of nonlinear phenomena, these simple fronts are found to be vulnerable to instabilities as discussed in section 6.

3.1. *A simple irreversible model*

Under conditions of low iron and high oxygen content in the inlet waters, we expect the overall redox process to be characterized by

$$m\mathrm{X} + n\mathrm{P} \xrightarrow{W} \text{products}. \tag{3.1}$$

The products of the oxidation of the mineral pyrite ($\mathrm{P} = \mathrm{FeS_2}$) by oxygen ($\mathrm{X} = \mathrm{O_2}$) are considered in greater detail in section 5 and in ref. 7. Briefly they include complexes of Fe^{3+} with OH^- and oxidized sulphur species like SO_4^{2-} and $S_2O_3^{2-}$. In (3.1) W represents the rate of the reaction and m and n are stoichiometric coefficients.

Reaction (3.1) is driven by the influx of oxygen dissolved in the water flowing with velocity $\boldsymbol{v}(\boldsymbol{r}, t)$ through the system. We assume the continuity equation

$$\frac{\partial X}{\partial t} = D\nabla^2 X - \nabla\cdot(X\boldsymbol{v}) - mW, \tag{3.2}$$

where X represents the O_2 concentration per rock volume, and D is the diffusion coefficient for oxygen. Since pyrite grains are immobile, the pyrite content P (in moles of pyrite/cm^3 of rock volume) evolves via

$$\frac{\partial P}{\partial t} = -nW. \tag{3.3}$$

To complete the description we need the initial data, $X(\boldsymbol{r}, 0)$ and $P(\boldsymbol{r}, 0)$ and the boundary conditions.

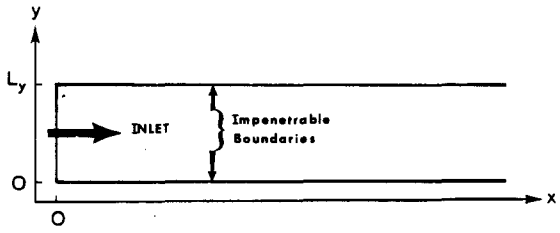

Fig. 3. Idealized two-dimensional lossless, constant cross section aquifer. The advancement velocity of redox fronts (when they exist) can be calculated exactly in great generality for such system – see section 3.

3.2. *The idealized aquifer*

An idealized case is shown in fig. 3. At the top and bottom surfaces the normal flux vanishes since the aquifer is assumed lossless. We take the water velocity in the x-direction along the aquifer. Although all results to follow hold for an aquifer of arbitrary cross section shape, we assume the aquifer to be rectangular for simplicity here. The no-flux boundary condition then becomes, assuming that v is along the x-direction only,

$$\frac{\partial X}{\partial y}=0, \quad y=0, L_y, \tag{3.4}$$

$$\frac{\partial X}{\partial z}=0, \quad z=0, L_z. \tag{3.5}$$

At the meteoric inlet, $x=0$, the concentration $X(0, y, z, t)$ is assumed to have the time-independent value $X_M(y, z)$,

$$X(0, y, z, t)=X_M(y, z). \tag{3.6}$$

Before the pyrite becomes oxidized P has its initial value $P_0(y, z)$ taken to be constant along the aquifer,

$$P(x, y, z, 0)=P_0(y, z). \tag{3.7}$$

Since the flow is in the x direction only, we have

$$v=v(y, z)x, \tag{3.8}$$

where x is a unit vector pointing along the aquifer away from the meteoric inlet (in the positive x direction).

3.3. *Constant-velocity redox fronts*

Far from the meteoric inlet the X and P profiles are monotone interlaced as shown in fig. 4. We expect that for the idealized case there can be a balance set up such that the total rate of oxidant moved in just eliminates a stoichiometric amount of pyrite such that the redox interface moves forward at a constant velocity denoted u. We now obtain an exact equation for u in this idealized aquifer.

It is convenient to study such a constant velocity solution in the reference frame $\varphi=x-ut$ moving with the front. In this wave-fixed frame $X=X(\varphi, y, z)$, $P=P(\varphi, y, z)$. Substituting these expressions into (3.2), (3.3), (3.4), (3.5) and taking account of the initial data, we find that the idealized redox front is described by the solution of the following problem:

$$D\left[\frac{\partial^2}{\partial\varphi^2}+\frac{\partial^2}{\partial y^2}+\frac{\partial^2}{\partial z^2}\right]X+(u-v)\frac{\partial X}{\partial\varphi}-mW=0, \tag{3.9}$$

$$u\frac{\partial P}{\partial\varphi}-nW=0, \tag{3.10}$$

$$\frac{\partial X}{\partial y}=0, \quad y=0, L_y, \tag{3.11}$$

$$\frac{\partial X}{\partial z}=0, \quad z=0, L_z, \tag{3.12}$$

$$X\widetilde{\varphi\to-\infty}\bar{X}_M, \quad X\widetilde{\varphi\to+\infty}0, \tag{3.13}$$

$$P\widetilde{\varphi\to-\infty}0, \quad P\widetilde{\varphi\to\infty}P_0(y, z), \tag{3.14}$$

where a bar atop any function $f(y, z)$ indicates the cross section average, i.e.

$$\bar{f}=\frac{1}{L_yL_z}\int_0^{L_y}dy\int_0^{L_z}dzf(y, z). \tag{3.15}$$

We have imposed the condition $X\to\bar{X}_M$ as $\varphi\to-\infty$ because far from the meteoric inlet, but far

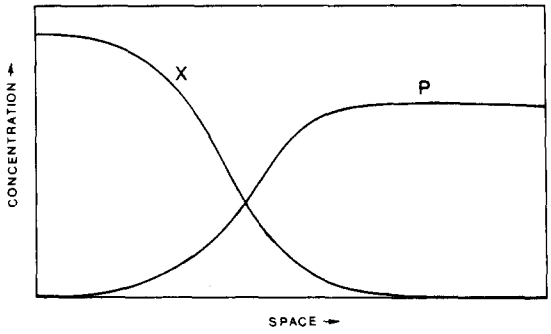

Fig. 4. Schematic interlaced X,P profiles for simple irreversible redox front as discussed in section 4.

behind the front, X has had time to become uniform through diffusion.

An analytical expression for u may be obtained. First we combine (3.9), (3.10) to get

$$D\left[\frac{\partial^2}{\partial\varphi^2}+\frac{\partial^2}{\partial y^2}+\frac{\partial^2}{\partial z^2}\right]X+(u-v)\frac{\partial X}{\partial\varphi}=\frac{mu}{n}\frac{\partial P}{\partial\varphi}. \tag{3.16}$$

Integrating both sides over a cross section area and using the no-flux boundary conditions (3.11), (3.12) we get

$$\frac{d}{d\varphi}\left[D\frac{d\bar{X}}{d\varphi}+u\bar{X}-\overline{vX}-\frac{mu\bar{P}_0}{n}\right]=0. \tag{3.17}$$

Hence the quantity in brackets is a constant over the front profile. Using (3.13), (3.14), we can evaluate the constant at $\varphi=-\infty$ and $+\infty$. Equating the two results we get

$$u=\frac{n\bar{X}_M\bar{v}}{n\bar{X}_M+m\bar{P}_0}. \tag{3.18}$$

In obtaining this result we have used the fact that far from the inlet but still well behind the front $\overline{Xv}$ is $\bar{X}_M\bar{v}$.

The result (3.18) has a simple physical interpretation. Rewriting it in the form

$$n(\bar{v}-u)\bar{X}_M=mu\bar{P}_0 \tag{3.19}$$

it states that, in the wave-fixed reference frame, the total amount of X moving into the redox interface from its downstream side equals the total stoichiometrically balanced amount of P moving in from the other side. Thus (3.18) is simply a result of the losslessness of the aquifer and the stoichiometry of the oxidation process (3.1). Also, u in (3.18) measures the capacity of the rock to buffer the water. If $\bar{P}_0 \ll \bar{X}_M$ the rock is unable to significantly buffer the water and the redox front will move as fast as the water ($u \approx \bar{v}$). In the typical case where $\bar{P}_0 \gg \bar{X}_M$ the rock has a high buffering capacity and hence the front will move much more slowly than the water ($u \ll \bar{v}$).

This result has been obtained assuming the existence of a constant velocity front. From the previous section we see that not all such water–rock interaction kinetic schemes yield constant velocity fronts. The above calculations yield a constant velocity front speed but do not prove its existence or stability. In the next section we determine solutions of certain constant velocity water–rock interaction fronts in various geologically important limiting cases. The exact result (3.18) can be generalized to much more complex systems with interesting consequences as will be seen in section 5.

4. Quasi-discontinuous fronts

Systems of low porosity have slow transport. In these transport-limited situations, the zone in which the redox processes take place is often narrow. In this section we develop equations for the speed and profile of these narrow transition fronts and set forth solutions in some simple cases.

4.1. *A simple irreversible model*

To illustrate the theory we consider the redox dynamics of section 3. The relatively high rate of reaction relative to transport is emphasized here by writing the rate of reaction W in (3.2), (3.3) as w/ϵ where $w(X, P)$ is a rate expression and $1/\epsilon$ is a large rate coefficient, i.e. $\epsilon \ll 1$. We thus examine

the solutions of (3.2), (3.3) in the formal limit $\epsilon \to 0$.

By the nature of process (3.1) we expect that w vanishes if either X or P does. Thus as $\epsilon \to 0$ the solutions of (3.2), (3.3), written here as

$$\frac{\partial X}{\partial t} = \nabla\cdot[D\nabla X - Xv] - mw/\epsilon, \tag{4.1}$$

$$\frac{\partial P}{\partial t} = -nw/\epsilon, \tag{4.2}$$

are expected to look qualitatively like fig. 5, i.e. space is divided into well-defined zones where $X \neq 0$, $P = 0$ – the oxidized zone – and where $X = 0$, $P \neq 0$ – the reduced zone. This must be true or else the solutions of (4.1), (4.2) must vary extremely rapidly in space or time if w is nonzero as $\epsilon \to 0$; in obtaining the above picture we have assumed that $w(X, P)$ vanishes as either X or P vanishes.

To describe the interface between these zones we introduce a function $E(\boldsymbol{r}, t)$ such that the reaction zone for small ϵ is a narrow domain centered about the surface defined by

$$E(\boldsymbol{r}, t) = 0. \tag{4.3}$$

We make the convention $E < 0$ in the oxidized region and $E > 0$ in the reduced domain. Our analysis will proceed by obtaining equations for X and P in their respective domains, coupled to an equation for E.

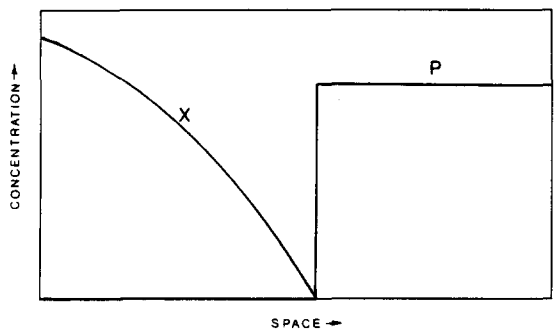

Fig. 5. Same as in fig. 4 except for the fast reaction limit.

The concentration profiles may be obtained most directly by combining (4.1), (4.2) in the form

$$\frac{n}{m}\left[\frac{\partial X}{\partial t} + \nabla\cdot(vX - D\nabla X)\right] = \frac{\partial P}{\partial t}. \tag{4.4}$$

In the oxidized region P vanishes as $\epsilon \to 0$ and X vanishes downstream from the redox interface Thus we have

$$\frac{\partial X}{\partial t} = \nabla\cdot(D\nabla X - vX), \quad E < 0, \tag{4.5}$$

$$X = 0, \qquad E > 0. \tag{4.6}$$

Since X vanishes in the reduced zone, we have the trivial equation $\partial P/\partial t = 0$. Thus P is constant and hence it remains at its initial value denoted $P_0(\boldsymbol{r})$. Thus

$$P = \begin{cases} 0, & E < 0, \\ P_0(\boldsymbol{r}), & E > 0. \end{cases} \tag{4.7}$$

To complete the theory we require an evolution equation for $E(\boldsymbol{r}, t)$ and boundary conditions for X at the redox interface. The former is obtained as follows. Let $\boldsymbol{n}$ be a unit normal to the redox interface $E = 0$ pointing into the reducing zone, i.e. $\boldsymbol{n} = \nabla E/|\nabla E|$. We define u as the velocity of advancement of the front in the direction $\boldsymbol{n}$. In a small time δt a point $\boldsymbol{r}$ on $E = 0$ moves to $\boldsymbol{r} + \boldsymbol{n}u\,\delta t$. The latter must, by definition, lie on $E(\boldsymbol{r} + u\,\delta t\boldsymbol{n}, t + \delta t) = 0$. Expanding the latter up to linear terms in the infinitesimal δt and noting $E(\boldsymbol{r}, t) = 0$, we get

$$\frac{\partial E}{\partial t} + u|\nabla E| = 0. \tag{4.8}$$

The advancement velocity u is given in terms of the normal flux of X as follows. In a time δt, $\boldsymbol{n}\cdot(vX - D\nabla X)\,\delta t\,\delta A$ moles of X pass across a small area δA on the redox interface $E = 0$. Because reaction is fast this consumes P in a small zone of area δA and width δL. The number of moles of P consumed is $nP_0\,\delta A\,\delta L/m$. Thus we have $\boldsymbol{n}\cdot(vX_0 - D\nabla X_0)\,\delta t = nP_0\,\delta L/m$. But since

$u = \delta L/\delta t$ we get

$$u = \frac{-mn \cdot D\nabla X}{nP_0}. \tag{4.9}$$

To obtain this result we have used the fact that since X is continuous it must vanish at $E = 0$ as $\epsilon \to 0$. Thus we have

$$\frac{\partial E}{\partial t} = \frac{mD}{nP_0(r)} \nabla X \cdot \nabla E, \tag{4.10}$$

the equation for the moving interface. Eqs. ((4.5)–(4.7), (4.10)) with the initial data and boundary conditions

$$X(r,0) \quad \text{in} \quad E(r,0) < 0, \tag{4.11}$$

$$X(r,t) = X_M(r) \text{ at meteoric inlet}, \tag{4.12}$$

$$X(r,t) = 0 \quad \text{on} \quad E(r,t) = 0 \tag{4.13}$$

and the function $E(r,0)$ constitute a well posed, free boundary problem [10, 11].

4.2. *Planar redox front solutions*

An exact solution for the redox interface described by ((4.5)–(4.7), refs. 10–13) can be obtained for the case of constant flow velocity v, meteoric oxygen concentration X_M and initial pyrite content P_0 (i.e. v, X_M and P_0 independent of r – see fig. 5). With $E = \varphi = x - ut$ for advancement along the x direction we obtain

$$X = \begin{cases} X_M[1 - \exp\{(v-u)\varphi/D\}], & x < ut, \\ 0, & x > ut. \end{cases} \tag{4.14}$$

The advancement velocity u of the redox front is obtained by inserting (4.14) into (4.10) with $E = x - ut$ to obtain

$$u = \frac{nX_M v}{nX_M + mP_0} \tag{4.15}$$

in agreement with the general result (3.18).

The profile in (4.14) demonstrates the effect of the competition between flow and diffusion. Because $u < v$ and φ is negative to the left of the front, we see that if D is small the second term in (4.14) is negligible and $X = X_M$ for $x < ut$ and $X = 0$ for $x > ut$; i.e. X is a step function. Thus in the regime where flow dominates diffusion the concentration drops abruptly at the redox interface. More generally D/v, the "upstream diffusion length", characterizes the width of the transition zone over which the incoming species may diffuse upstream from the zone where fast solid reactions occur.

4.3. *Fast reversible redox dissolution front*

We next contrast the above irreversible redox front with a related reversible one. Consider X-laden waters flushing through an aquifer containing the solid P and reacting according to

$$m\mathrm{X} + n\mathrm{P} \overset{w/\epsilon}{\leftrightarrows} y\mathrm{Y} + z\mathrm{Z}, \tag{4.16}$$

where Y and Z are mobile species and y and z are stoichiometric coefficients. We now investigate this reversible process in the limit of fast equilibration, $\epsilon \to 0$.

Assume that w has the form

$$w = kP^{\beta} R(X, Y, Z), \tag{4.17}$$

where at equilibrium, $R = 0$, we have

$$X = X^{eq}(Y, Z). \tag{4.18}$$

In particular, for low concentrations we have $(X^{eq})^m = KY^yZ^z$, where K is the equilibrium constant for (4.16). Finally the exponent β is positive and, for surface area limited kinetics, is $2/3$.

As $\epsilon \to 0$ space is again divided into two regions:

$$P = 0, \quad E(r,t) < 0, \tag{4.19}$$

$$P \neq 0, \quad X = X^{eq}(Y,Z), \quad E(r,t) > 0. \tag{4.20}$$

The interface $E = 0$ moves with (4.8) in general, but for the reversible problem, the equations for E and u, are implicit as follows. Across the boundary $E = 0$, X, Y and Z are continuous, i.e.

$$X(0^-) = X(0^+) \tag{4.21}$$

and similarly for Y and Z. The notation 0^+ and 0^- implies evaluation at points very close to $E = 0$, i.e. $E = 0^+$ or 0^- where 0^+ and 0^- are very small positive and negative numbers respectively. Using scaling methods [11, 12], we can obtain expressions for the jumps in the normal derivatives of X, Y and Z across the boundary, namely

$$n[\boldsymbol{n} \cdot D_X \nabla X]_{0^-}^{0^+} + uP(0^+) = 0, \tag{4.22}$$

$$n[\boldsymbol{n} \cdot D_Y \nabla Y]_{0^-}^{0^+} - yuP(0^+) = 0, \tag{4.23}$$

$$n[\boldsymbol{n} \cdot D_Z \nabla Z]_{0^-}^{0^+} - zuP(0^+) = 0, \tag{4.24}$$

where $\boldsymbol{n} = \nabla E / |\nabla E|$, and we have noted P is zero for $E < 0$ (i.e. $P(0^-) = 0$).

The conservation equations for X, Y and Z in the two domains can be readily obtained. For $E < 0$ P vanishes and hence from (4.4) we have

$$\frac{\partial X}{\partial t} = D_X \nabla^2 X - \nabla \cdot (vX), \quad E < 0 \tag{4.25}$$

and similarly for Y and Z. In the reduced zone, $E > 0$, $P \neq 0$. Because $X = X^{eq}(Y, Z)$ in $E > 0$ we can get closed equations for Y and Z by solving for w/ϵ in the conservation equation for X and then using $X = X^{eq}(Y, Z)$ in the equations for Y and Z to express the w/ϵ factor in terms of Y and Z. We get

$$\frac{\partial Y}{\partial t} = D_Y \nabla^2 Y - \nabla \cdot (vY) + \frac{y}{m}\left[\frac{\partial X^{eq}}{\partial t} - D_X \nabla^2 X^{eq} + \nabla \cdot (vX^{eq})\right], \tag{4.26}$$

$$\frac{\partial Z}{\partial t} = D_Z \nabla^2 Z - \nabla \cdot (vY) + \frac{z}{m}\left[\frac{\partial X^{eq}}{\partial t} - D_X \nabla^2 X^{eq} + \nabla \cdot (vX^{eq})\right]. \tag{4.27}$$

Once Y and Z are obtained from (4.26), (4.27) we can calculate P via

$$\frac{\partial P}{\partial t} = -\frac{n}{m}\left[\frac{\partial X^{eq}}{\partial t} - D_X \nabla^2 X^{eq} + \nabla \cdot (vX^{eq})\right]. \tag{4.28}$$

This completes the general description of the fast equilibrium redox dissolution front when the dynamics of E is represented by (4.8).

Note the interesting difference between the structure of this free boundary problem and that of the free boundary dynamics of the previous section wherein the reduced domain ($E > 0$) problem was trivial ($X = 0$ for $E > 0$). In the present problem P need not be constant for $E > 0$; indeed P dissolves or grows just enough to ensure that $X = X^{eq}(Y, Z)$ in $E > 0$. Furthermore note that while (4.26), (4.27) look like modified transport equations for a reaction-free system, their structure does allow for sinks or sources of Y and Z to account for P dissolution or precipitation.

4.4. *The planar reversible redox front*

The problem of the previous section yields a constant velocity propagating interface. Assume the flow is in the x-direction and the advancement speed is u. Then in the wave fixed frame $\varphi = x - ut$, we have, putting the interface at $\varphi = 0$,

$$D_X X'' + (u - v) X' = 0, \quad \varphi < 0, \tag{4.29}$$

and similarly for Y and Z. These equations yield a solution of the form

$$\begin{aligned} X(\varphi) &= X_M + A\, e^{(v-u)\varphi/D_X}, \\ Y(\varphi) &= B\, e^{(v-u)\varphi/D_Y}, \\ Z(\varphi) &= C\, e^{(v-u)\varphi/D_Z}, \end{aligned} \tag{4.30}$$

assuming that at the meteoric inlet (here at $\varphi = -\infty$), Y and Z are negligible. The constants A, B, C will be determined below.

The continuity condition for X, Y and Z and the equilibrium relation $X = X^{eq}(Y, Z)$ for $\varphi = 0^+$

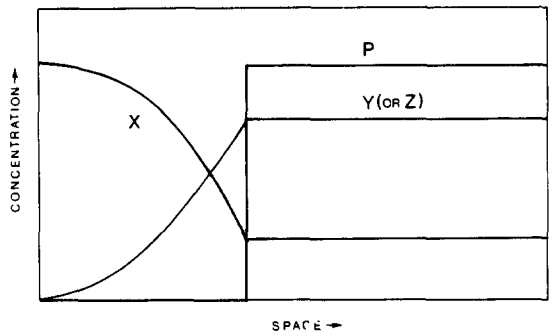

Fig. 6. Same as in fig. 5 except for the reversible simple model of section 4 in the fast reaction limit.

together yield

$$X_M + A = X^{eq}(B, C),$$
$$B = Y(0^+), \tag{4.31}$$
$$C = Z(0^+).$$

We now show that if all variables are constant for $\varphi > 0$, clearly a solution of (4.26)–(4.28), all necessary conditions can be satisfied and indeed the advancement velocity u can be determined. The derivative discontinuity relations (4.22)–(4.24) yield

$$-n(v-u)A - muP_0 = 0,$$
$$-n(v-u)B + yuP_0 = 0, \tag{4.32}$$
$$-n(v-u)C + zuP_0 = 0.$$

Note that since we seek solutions such that all variables are constant for $\varphi > 0$, we have set P equal to its (assumed) constant initial value P_0. Eqs. (4.31), (4.32) are six equations in the six unknowns A, B, C, $Y(0^+)$, $Z(0^+)$ and u.

An equation for u can be obtained by combining the above results; we find

$$X^{eq}\left[\frac{y}{n}\mu, \frac{z}{n}\mu\right] + \frac{m}{n}\mu = X_M, \tag{4.33}$$
$$\mu = uP_0/(v-u).$$

The simple case $X + P = Y$ yields

$$u = X_M v/[X_M + (1+K)P_0] \tag{4.34}$$

when the equilibrium concentration of X takes on the low concentration limiting behavior $X^{eq} = KY$ where K is the equilibrium constant. This agrees with the irreversible case of section 4.2 (see (4.15)) when we take the irreversible limit $K \to 0$. The concentration profiles are shown schematically in fig. 6. As $K \to 0$, $X(0^+) \to 0$, and the reversible profile maps onto the irreversible one.

For non-ideal systems the equation for u, (4.33), could have multiple solutions corresponding to multiple types of waves. This discrete multiplicity is in contrast to the possible existence of a one-parameter family of waves (continuous multiplicity) for the two-mineral model of the next section. Clearly, discrete multiplicity is possible in the above reversible front whenever $X^{eq}(y\mu/n, z\mu/n)$ as a function of μ has a sufficiently sharp maximum. This could in principle happen for non-ideal equilibrium relations.

4.5. *Nonlinear phenomena at redox fronts*

Having obtained planar redox front solutions, we are led to the investigation of their stability. In a companion paper, ref. 13, we find that the simple irreversible front is stable both among the class of planar solutions (in fact, globally so) and linearly morphologically stable (i.e., with respect to changes of shape). Rigorous results on existence and uniqueness are also given there for the irreversible case.

Morphological instability is found, however, when the reactive flows induce changes in porosity which, in turn, couple to the flow v via Darcy's law – see ref. 14 for details. From these results and the possibility of discrete multiplicity for the reversible front, it is clear that water–rock interaction fronts can support a host of nonlinear phenomena including dynamical behavior as discussed in section 7 below.

5. Two-mineral replacement front

5.1. *The model*

Perhaps the simplest model that describes the iron–sulfur redox chemistry is summarized as follows:

$$\tfrac{3}{2}O_2 + FeS_2(\text{Pyrite}) = Fe^{2+} + S_2O_3^{2-}, \tag{5.1}$$

$$\tfrac{1}{4}O_2 + \tfrac{3}{2}H_2O + Fe^{2+} = FeO \cdot OH(\text{Goethite}) + 2H^+. \tag{5.2}$$

In the presence of buffering reactions H^+ tends to have a fixed value and we assume this to be the case. Since H_2O is in excess in the aqueous environment, it can be neglected in a schematic kinetics and thus we arrive at the following simplified working model:

$$a\mathrm{X} + \mathrm{P} = \mathrm{F} + \mathrm{T}, \tag{5.3}$$

$$b\mathrm{X} + \mathrm{F} = \mathrm{G}, \tag{5.4}$$

where X, F and T are the mobile species (O_2, Fe^{2+} and $S_2O_3^{2-}$); P and G represent pyrite and goethite respectively. The stoichiometric parameters a and b are 3/2 and 1/4 respectively, but to simplify the analysis while still maintaining the interesting effects we shall take $a = b = 1$.

Let W_1 and W_2 be the overall rate laws of processes (5.3), (5.4). They are presumed expressible as functions of X, F, T, P and G. At equilibrium these rates must yield the correct equilibrium relations

$$KX = FT, \quad W_1 = 0, \tag{5.5}$$

$$Q = FX, \quad W_2 = 0; \tag{5.6}$$

here K and Q are equilibrium constants, and we assume the solution to be dilute.

Consider a one-dimensional, lossless, initially homogeneous aquifer with oxidizing waters entering from the left. Then for a front of P dissolution and G deposition we impose the following conditions on either side of and far from the transition region where (5.3) and (5.4) are operative:

$$\begin{aligned} &P(-\infty) = G(+\infty) = 0, \\ &P(+\infty) = P_0, \quad G(-\infty) = (1-\alpha)P_0, \\ &X(-\infty) = X_M, \quad F(-\infty) = F_M, \quad T(-\infty) = 0, \\ &X(+\infty) = X_\infty, \quad F(+\infty) = F_\infty, \quad T(+\infty) = T_\infty. \end{aligned} \tag{5.7}$$

P_0 is the pyrite content in the unoxidized aquifer. The amount of iron fixed as goethite is $(1-\alpha)P_0$, $\alpha \le 1$, defining α. The incoming (meteoric) iron and oxygen are F_M and X_M respectively. The downstream values X_∞, F_∞ and T_∞ are determined for steady front propagation as we shall see below.

Far in advance of and behind the front the waters have had time to come to equilibrium with local rocks. Thus we assume the following connections:

$$\begin{aligned} &F_\infty T_\infty = KX_\infty, \\ &F_M X_M = Q, \quad \alpha < 1 \quad \text{(G-saturated inlet)}, \\ &F_M X_M < Q, \quad \alpha = 1 \quad \text{(G-undersaturated inlet)}, \end{aligned} \tag{5.8}$$

which follow directly from the data (5.7) and the equilibrium conditions (5.5), (5.6). Note that if the inlet waters are undersaturated with respect to goethite then the last condition in (5.8) holds and $\alpha = 1$ (and hence $G(-\infty) = 0$).

Our goal in this section is to investigate the steady state advancement of a pyrite–goethite front due to the mechanism (5.3), (5.4). Assuming the existence of such a front we now show how some of its properties can be determined quite easily without actually calculating the composition profiles.

In the frame moving with the redox front at velocity u, (i.e. $\varphi = x - ut$ is the redox front-fixed reference frame) we have

$$uP' - W_1 = 0, \tag{5.9}$$

$$uG' + W_2 = 0, \tag{5.10}$$

$$D_X X'' + (u - v)X' - W_1 - W_2 = 0, \tag{5.11}$$

$$D_F F'' + (u - v)F' + W_1 - W_2 = 0, \tag{5.12}$$

$$D_T T'' + (u - v)T' + W_1 = 0, \tag{5.13}$$

where "′" = d/dφ. Eqs. (5.7)–(5.13) provide a complete description of the steady state front once the functional forms of W_1 and W_2 are set forth.

5.2. *Constants of the front motion*

Three constants of the motion for redox front advancement can be obtained by eliminating W_1 and W_2 from the five equations (5.9)–(5.13). We find

$$[D_X X' + (u-v)X + u(G-P)]' = 0, \tag{5.14}$$

$$[D_F F' + (u-v)F + u(P+G)]' = 0, \tag{5.15}$$

$$[D_T T' + (u-v)T + uP]' = 0. \tag{5.16}$$

From this we see that the quantities inside the brackets are constants over the steady state wave profile. Evaluating each of these constants at $\varphi = -\infty$ and $\varphi = +\infty$ and equating the results, using the P equilibrium relation at $\varphi = \infty$, and eliminating T_∞, we obtain

$$(u-v)X_M = (u-v)X_\infty - u(2-\alpha)P_0, \tag{5.17}$$

$$(u-v)F_M = -(u-v)^2 \frac{KX_\infty}{uP_0} + u\alpha P_0. \tag{5.18}$$

These results may be further combined to obtain an equation relating u and α:

$$\alpha(u) = \frac{(u-v)\{F_M uP_0 + K[(u-v)X_M + 2uP_0]\}}{uP_0\{uP_0 + (u-v)K\}}. \tag{5.19}$$

With this we may then obtain the other unknowns,

$$X_\infty(u) = (u-v)^{-1}[(u-v)X_M + u(2-\alpha(u))P_0], \tag{5.20}$$

$$F_\infty(u) = -(u-v)KX_\infty(u)/uP_0. \tag{5.21}$$

These results are interesting. They indicate that the redox front solutions of our model for the saturated inlet are not necessarily unique but may constitute a one-parameter family of solutions that differ according to their velocity u. This type of behavior is not unknown in other problems, most notably the Fisher equation of ecology. In the Fisher problem, it is found that only one velocity corresponds to a stable wave.

5.3. *Constraints on allowed velocities for the saturated case*

5.3.1. *Positivity constraints*

The positivity of concentrations puts constraints on the allowed range of u values. Since $G(-\infty) \geq 0$,

$$\alpha(u) \leq 1. \tag{5.22}$$

Also $F(+\infty) > 0$ implies that

$$u < v. \tag{5.23}$$

Most interesting is the condition $X_\infty > 0$; this implies

$$\alpha(u) \geq \alpha_B(u) \equiv \frac{(u-v)X_M + 2uP_0}{uP_0}. \tag{5.24}$$

These inequalities place constraints on the allowed values of u.

5.3.2. *Poles and zeros of $\alpha(u)$ and $\alpha_B(u)$*

The curve $\alpha(u)$ of (5.19) with $F_M = Q/X_M$ has several features that dominate its behavior and which, along with the constraints, point out the existence of two distinct domains of behavior. The zeros of $\alpha(u)$ occur at $u = v$, u_0 where

$$u_0 \equiv \frac{KX_M^2 v}{KX_M^2 + 2KP_0X_M + QP_0}. \tag{5.25}$$

Also there are two poles of $\alpha(u)$ located at $u = 0$, u_P where

$$u_P \equiv \frac{Kv}{K + P_0}. \tag{5.26}$$

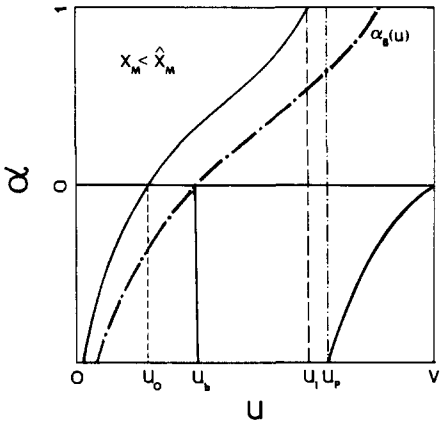

Fig. 7. Schematic plot of α-parameter as a function of the wave speed u of the pyrite-goethite model. As discussed in section 5 this figure demonstrates the possible existence of a continuum of fronts with different values of the amount of goethite deposited (as measured by α).

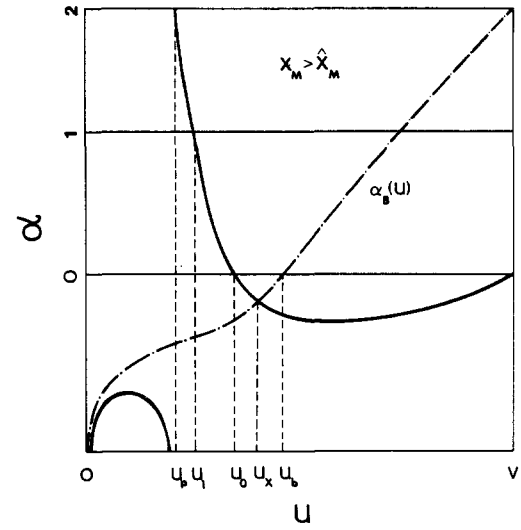

Fig. 8. Same as in fig. 7 except for a different range of inlet X (see section 5 for details).

The curve $\alpha_B(u)$ has a zero at u_b,

$$u_b \equiv \frac{X_M v}{X_M + 2P_0}. \tag{5.27}$$

The inequality

$$u_b > u_0 \tag{5.28}$$

follows from (5.25), (5.27).

From these results it is seen that there are two distinct cases, depending on whether the pole of $\alpha(u)$ is to the right or left of its zero, i.e. $u_P \gtrless u_0$. The two cases are shown schematically in figs. 7 and 8.

5.3.3. *Two regimes of front propagation*

a) Case $u_P > u_0$. The expressions for u_P and u_0 of the previous section yield for this case

$$X_M^2 - 2KX_M - Q < 0. \tag{5.29}$$

Since $X_M > 0$, this condition reduces to

$$0 \le X_M < \hat{X}_M \equiv K + [K^2 + Q]^{1/2}. \tag{5.30}$$

The curves $\alpha(u)$ and $\alpha_B(u)$ are shown in fig. 7 for this case. It is seen that since $\alpha > \alpha_B$ the allowed values of u lie in the interval $0 < u < u_1$ where $\alpha(u_1) = 1$.

b) Case $u_P < u_0$. This situation is seen in fig. 8. Since $\alpha > \alpha_B$ and $\alpha \le 1$ we see that the allowed velocities are in the interval $u_1 < u < u_x$ where u_x is the value of u at which α crosses α_B, namely

$$u_x = \frac{v(X_M^2 - Q)}{X_M^2 + 2P_0 X_M - Q}. \tag{5.31}$$

Because for this case

$$X_M > \hat{X}_M, \tag{5.32}$$

we see that both the numerator and denominator of u_x in (5.31) are positive and hence u is restricted to a finite domain. From fig. 8 we see that α lies in the range $1 > \alpha > \alpha_B(u_x)$ and if $u_x > u_0$ then α can be negative. In the latter case this would mean that the amount of G left behind the front, $G(-\infty) = (1-\alpha)P_0$, could exceed the original amount of pyrite, P_0, by extracting some iron from the inlet waters. Hence the present considerations do not rule out the possibility that $G(-\infty)$ exceeds P_0.

5.3.4. *Remarks*

Physically the one-parameter family of waves arises because the entry waters are in equilibrium with the final product G of the oxidation. The key question remaining concerns the existence and stability of each wave in the family; this is addressed numerically in the next section.

5.4. *Uniqueness for the undersaturated inlet*

For undersaturated inlet water $G(-\infty)=0$, and hence $\alpha=1$. Thus putting $\alpha=1$ in (5.19) yields a unique positive value of u, as the solution of

$$\left[P_0^2-K(P_0+X_M)-P_0F_M\right]u^2 + v\left[K(P_0+2X_M)+P_0F_M\right]u-KX_Mv^2=0. \tag{5.33}$$

Letting $A\equiv P_0^2-K[P_0+X_M]-P_0F_M$, we have

$$u=\frac{v}{2A}\left\{P_0\left[(K+F_M)^2+4KX_M\right]^{1/2} -K(P_0+2X_M)-P_0F_M\right\}. \tag{5.34}$$

Note that the zero in the denominator A is just cancelled by a zero in the numerator so that $u(X_M, F_M, P_0)$ is well behaved for all values of the parameters. The speed of the undersaturated inlet front is monotonically increasing from 0 to v as X_M varies from 0 to ∞.

It is interesting to note that the behavior of the front depends on the nature of the reaction. Thus the conclusion that u vanishes when X_M does would be altered if there was a process for pyrite dissolution that does not require oxygen (such as pyrite $\rightleftarrows Fe^{2+}+S_2^{2-}$). Such a "two-channel" dissolution front could also be analyzed by the conservation condition methods. For the case of goethite-undersaturated inlet water the total amount of goethite precipitated depends sensitively on the kinetic and transport rate laws, and not just on stoichiometry and equilibrium conditions.

6. Numerical simulation of the pyrite–goethite model

6.1. *Open questions*

The results of the previous sections lead us to a number of interesting questions. The possibility represented by (5.19) of a continuum of planar redox front solutions for the pyrite–goethite system raises the question of which among such a continuum exists and is stable. What is the exact nature of the critical value $\hat{X}_M$ of the inlet oxygen? Also, for the pyrite–goethite and the simple pyrite models of section 3 we would like to know about the stability to nonplanar perturbations – i.e. do there exist morphological instabilities of the planar front to the formation of scalloping or fingering?

To answer these questions we have undertaken a numerical study of these redox fronts. The numerical technique used is based on the usual spatial gridding and then solution of the resulting set of ordinary differential equations for the concentrations at each spatial grid point via a modified Euler method. We found a number of interesting results and surprises. The simulations presented here are limited to one-dimensional systems for the pyrite–goethite system of section 5. Two-dimensional simulations and analytical results on nonlinear and morphological stability analysis are presented elsewhere [13, 14].

6.2. *The detailed model*

The mechanism of the redox front studied here is as in section 5 for the special case $a=b=1$:

$$X+P \overset{W_1}{\rightleftarrows} F+T, \tag{6.1}$$

$$X+F \overset{W_2}{\rightleftarrows} G. \tag{6.2}$$

The rates of these reactions, W_1 and W_2, are constructed to include the following factors:

1) the rate vanishes at equilibrium;

2) the rate is proportional to the surface area of the mineral involved; and

3) nucleation of a new mineral occurs when a critical value of the appropriate concentration product (such as XF) is exceeded.

In the appendix we develop detailed mineral reaction rate laws based on the assumption that P and G occur as coatings on preexisting ("host") grains of an inert and predominant mineral constituting the porous rock. The rates are in the following forms:

$$W_1 = k(P+p)^{2/3}(KX - FT), \tag{6.3}$$

$$W_2 = q(G+g)^{2/3}(FX - Q). \tag{6.4}$$

The factors k and q are rate constants, K and Q are equilibrium constants, and p and g model nucleation effects. If $g = 0$ then, if there is no initial G, W_2 will always be zero and G will remain zero henceforth. Thus we let

$$g = \begin{cases} 0, & XF < Q_n \text{ and } G = 0, \\ g_0, & \text{otherwise}, \end{cases} \tag{6.5}$$

where $Q_n (> Q)$ is the threshold value of XF at which nucleation just starts and g_0 is a constant that depends sensitively on the original medium. If nucleation occurs readily on the host grain surfaces, g_0 will be large (reflecting all the host grain surface area) and Q_n will be near Q. Alternatively if G nucleation occurs at very rare surface defects on the host grains, then g_0 is small; Q_n can be near or much greater than Q depending on how easily G can nucleate at these selected sites. Similar considerations hold for p in modeling pyrite nucleation, i.e.

$$p = \begin{cases} 0, & (FT/X) < K_n, \quad P = 0, \\ p_0, & \text{otherwise}. \end{cases} \tag{6.6}$$

All simulations were carried out using the boundary and initial data for a one-dimensional system along the r-spatial coordinate in the interval $0 < r < L$. We took the inlet to be placed at $r = 0$ and chose the boundary condition at $r = L$ to simulate a semi-infinite system as follows:

$$\begin{aligned} &X(0,t) = X_M, \quad F(0,t) = F_M, \quad T(0,t) = 0; \\ &\frac{\partial X}{\partial r} = \frac{\partial F}{\partial r} = \frac{\partial T}{\partial r} = 0 \text{ at } r = L; \\ &X(r,0) = X_0, \quad F(r,0) = F_0, \quad T(r,0) = T_0, \\ &P(r,0) = P_0, \quad G(r,0) = 0. \end{aligned} \tag{6.7}$$

The initial concentrations X_0, F_0 and T_0 are assumed to be in equilibrium with pyrite, the solutes F and T assumed to have formed solely from reaction (6.1), i.e.

$$KX_0 = F_0 T_0, \quad F_0 = T_0. \tag{6.8}$$

Simulations differed according to the choices of X_M, F_M, K, Q, g_0, p_0, P_0, K_n, Q_n, and X_0, the aqueous flow velocity ($v > 0$), and the diffusion coefficients D_X, D_F, D_T.

The system was taken to evolve according to the following reaction–transport equations:

$$\frac{\partial X}{\partial t} = D_X \frac{\partial^2 X}{\partial r^2} - v\frac{\partial X}{\partial r} - W_1 - W_2, \tag{6.9}$$

$$\frac{\partial F}{\partial t} = D_F \frac{\partial^2 F}{\partial r^2} - v\frac{\partial F}{\partial r} + W_1 - W_2, \tag{6.10}$$

$$\frac{\partial T}{\partial t} = D_T \frac{\partial^2 T}{\partial r^2} - v\frac{\partial T}{\partial r} + W_1, \tag{6.11}$$

$$\frac{\partial P}{\partial t} = -W_1, \tag{6.12}$$

$$\frac{\partial G}{\partial t} = W_2. \tag{6.13}$$

These equations are the basis of the steady front equations (5.9)–(5.13) of the previous section.

6.3. *Undersaturated inlet* $F_M X_M < Q$

Using the above strategy, the undersaturated inlet waters case, $X_M F_M < Q$, was simulated numerically. A typical example is seen in fig. 9. Note that although goethite G nucleates and grows, it is eventually dissolved out by the waters undersaturated with respect to it. The theory of section

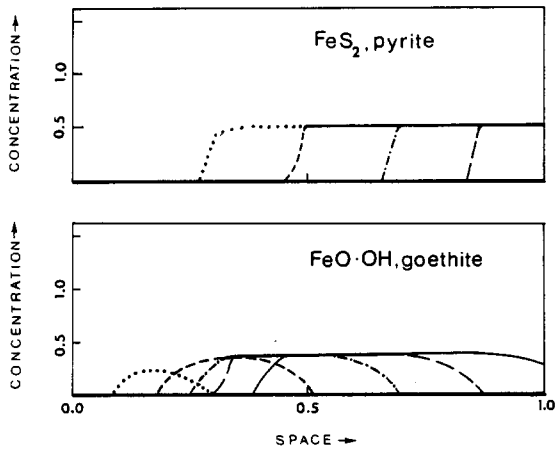

Fig. 9. Deposition and dissolution of goethite (G) in a redox front with inlet waters undersaturated with goethite. Parameter choices are $v = D_X = D_F = D_T = K = Q = P_0 = 1.0$; $k = 100$, $q = 10$; $X_M = 5.0$, $F_M = T_M = 0$, $Q_n = 1.1$. The spatial discretization increment is 0.05.

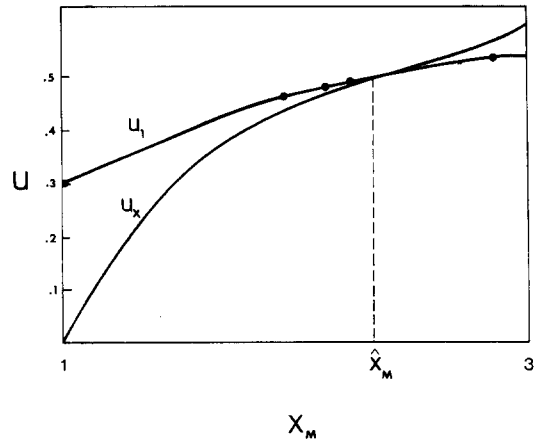

Fig. 10. Comparison of observed velocity (indicated by dots) and the bounds u_x and u_1. All parameter values are as in fig. 11 except that X_M is as shown here.

5.4 can be used to calculate the unique front speed when the inlet waters are not in goethite equilibrium. For the case $F_M = 0$ we obtain u from (5.34) as the unique positive solution. This relation was tested for various values of the other system parameters. It was found to hold when compared with the rate of advancement of the half height of the pyrite front obtained numerically.

6.4. *Selection from the continuum for* $F_M X_M = Q$

In the case of goethite-saturated inlet waters, the possible existence of a one-parameter family of fronts was demonstrated in section 5 (see (5.19)). Simulations were carried out to test this possibility and to see if any insight could be gained as to which wave (if any) was selected.

Results on the front advancement rate as a function of X_M are shown in fig. 10 for fixed values of the other parameters. Note that within the error of the calculation the observed speed always lies inside the allowed range predicted in section 5. In fact the observed velocities lie close to the limiting velocity u_1 for which $G(-\infty) = 0$.

Geologically we might argue that the original meteoric water that flows over a finite distance through surface rock does not quite dissolve enough G that saturation, $F_M X_M = Q$, is attained. Thus, because strictly speaking equilibrium takes an infinite time to be established, F_M is expected to be at most very close to but just below Q/X_M. In this spirit consider the conjecture that the physically relevant velocity u_{ob} can be obtained by calculating u for arbitrary F_M $(< Q/X_M)$ and then taking the limit as F_M approaches its goethite equilibrium value Q/X_M:

$$u_{ob} = \lim_{F_M \underset{<}{\to} \frac{Q}{X_M}} u(F_M). \tag{6.14}$$

The " $<$ " notation means that the approach of F_M to its equilibrium value Q/X_M is via a sequence of undersaturated values $F_M < Q/X_M$. For each such F_M, u has a unique value – there is no one-parameter family of fronts as for $F_M = Q/X_M$. Any goethite precipitated is eventually dissolved out since $F_M X_M < Q$; hence $G(-\infty) = 0$, $\alpha = 1$. Carrying out this undersaturated approach to equilibrium we find that u_{ob} is given by (5.34) with $F_M = Q/X_M$.

A qualitative argument for the instability of fronts for $\alpha < 1$ is as follows. Suppose $\alpha < 1$. Consider a point far behind the front; there

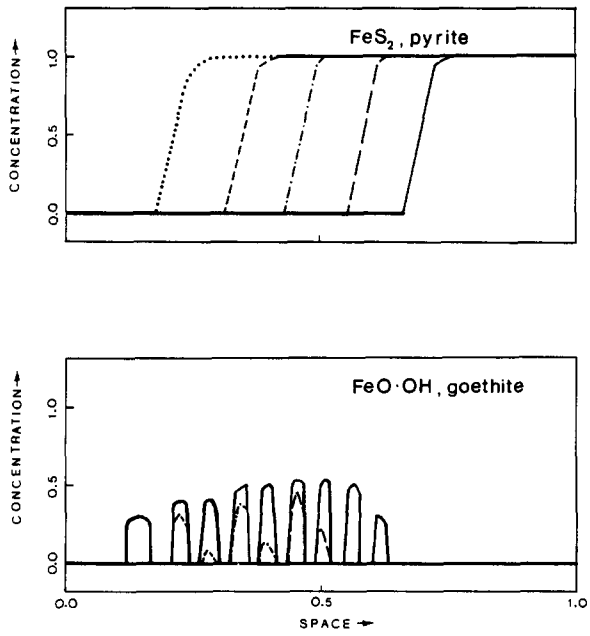

Fig. 11. Pyrite dissolution and oscillatory goethite deposition predicted from simulations as per section 6. Parameter values are $v = D_F = D_T = D_Z = K = Q = P_0 = 1.0$; $k = q = 10.0$; $X_M = 2.0$; $Q_n = 1.1$. The spatial increment used is 0.05. The various line patterns correspond to successive times.

goethite is bathed in saturated waters. At this point a fluctuation in the G growth rate could cause G to increase or decrease a little. If it dissolves then the flow will carry the excess F and X downstream. If G ever goes to zero by a series of such fluctuations then it will stay at zero unless a large fluctuation occurs such that $FX > Q_n$. This is highly improbable so that G in the wake of the front eventually finds its way to zero.

6.5. *Oscillatory deposition*

6.5.1. *The supersaturation, nucleation, depletion cycle*

Fig. 11 shows a striking, banded precipitation of goethite. This periodic deposition can be readily understood in terms of the original Ostwald theory of Liesegang banding [15]. For the present problem the Ostwald picture is as follows. When the product XF reaches its nucleation threshold, Q_n, goethite

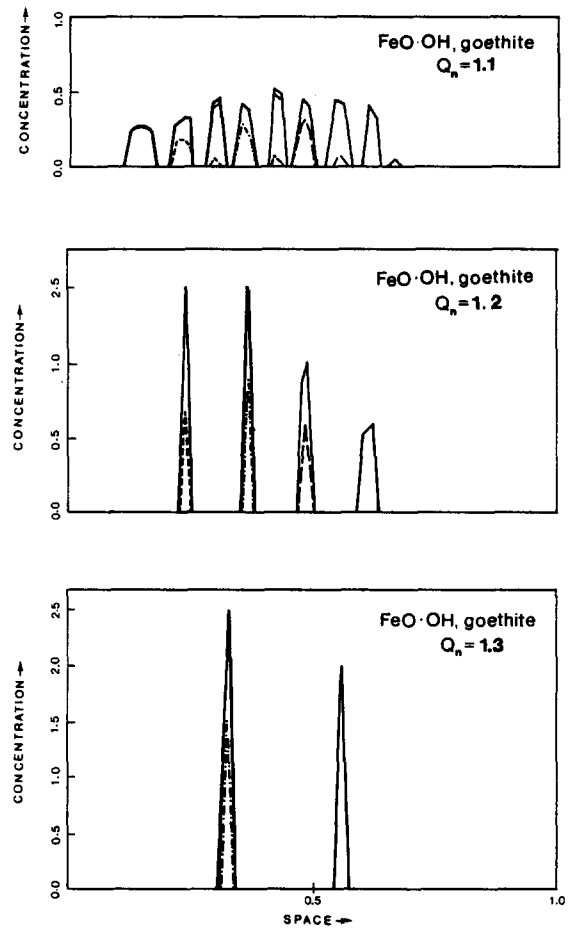

Fig. 12. Goethite deposition for parameters as in fig. 11 except for values of Q_n as indicated. Note dependence of amplitude and wavelength on Q_n.

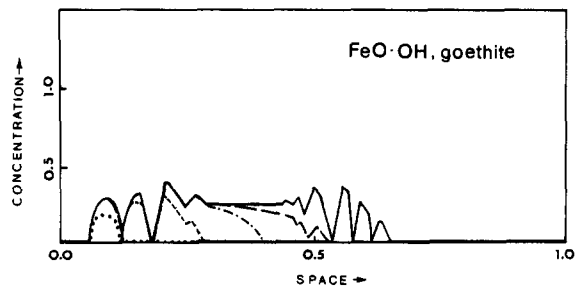

Fig. 13. Goethite deposition for the parameter values as in fig. 11 except $D_F = 0.5$. There are both goethite gaps (places where $G = 0$) and smooth oscillatory deposition of G. Note also that banding starts, stops and then starts again – an unexpected sequence. The various line patterns correspond to successive times.

precipitation begins. This causes depletion of F and X downstream so that nucleation may be repressed downstream until the pyrite front moves sufficiently far downstream that upstream diffusion to the original band is ineffective and hence the product XF again builds up. Further downstream XF attains its threshold value Q_n and a second region of G precipitate is nucleated. The cycle can clearly be repeated and explains the periodic precipitation of fig. 11.

In fig. 12 we show the dependence of the band spacing and amplitude on the nucleation threshold Q_n (see (6.4), (6.5)). Beyond a maximum value of Q_n no G precipitation is found since Q_n could never be exceeded by XF. As one might expect this maximum value of Q_n is of order (but less than) $X_M^{3/2}K^{1/2}$. We arrive at this estimate by noting that $X < X_M$ and that $(KX_M)^{1/2}$ is the value that F would attain if P was placed in waters initially free of F and T and with X at X_M. The simulations indicate that as Q_n reaches the cutoff value, the spacing diverges. Furthermore there is a lower value of Q_n below which banding gives way to unbanded precipitation.

There exists a transition between discrete banding (with G-free gaps between G-bearing bands) and undulatory continuous precipitation that seems sharp with respect to variations in X_M although the finite space grid increment may mask a more gradual transition. In this regard, we have carried out a series of runs at fixed parameters but with variable grid spacing and found that well-defined limiting profiles are attained as the grid is refined. The gap width attains a well defined limit as the space grid increment is decreased.

6.5.2. *Non-gap banding*

Under some conditions the effective diffusion of the aqueous iron species F through the rock could be quite slow because F could stick to the walls of the pores. This led us to try runs at various values of $D_F < D_X = D_T$. An interesting case is shown in fig. 13 where two types of banding are observed. Indeed, banding in our supersaturation/nucleation/depletion mathematical model does not occur only with precipitate free gaps – unlike the Prager formulation [16] of the Ostwald theory. Another way to get non-gap banding is by the competitive particle growth model based on the surface tension-mediated dependence of the equilibrium constant on particle size [17, 18]. A further advantage of the present model over the Prager formulation is that the finite width and profile of the bands may be predicted.

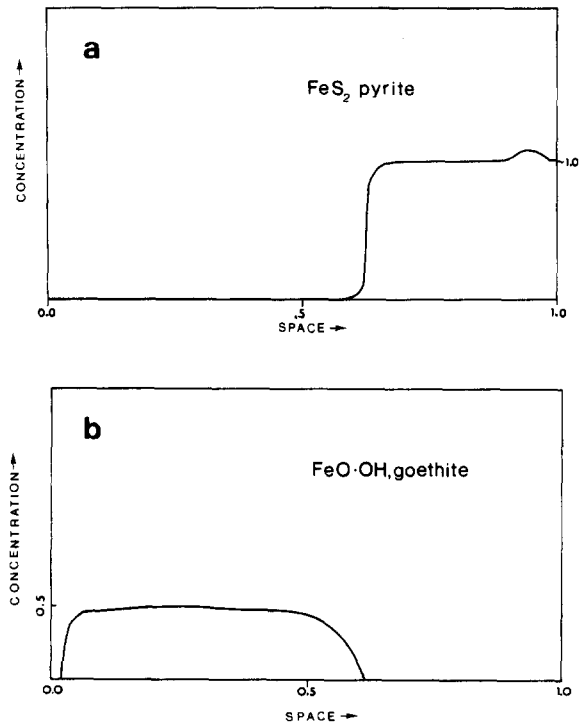

Fig. 14. Pyrite (a) and Goethite (b) evolution for parameters the same as fig. 11 except $D_X = 0.1$. Note the maximum of P (secondary pyrite deposition) reminiscent of the pyrite deposition zone just ahead of the front in the geological system of fig. 1.

6.6. *Reprecipitation of pyrite*

In all the simulations shown thus far, the profile of P has simply been a monotonic front from 0 to P_0. However, in some roll type deposits (fig. 1),

FeS_2 is observed to have a maximum just downstream of the redox front. This FeS_2 crest is manifest in our simulation of fig. 14, reminiscent of the geological example of fig. 1.

Appendix

The specific form of grain growth/dissolution laws depends on a number of detailed considerations. Here we take the case where the active minerals form as a coating on inert, host grains. We develop the formulae for a mineral G that forms from aqueous species X and F via X + F = G as in sections 5 and 6.

Consider spherical host grains of radius R_0. When G overgrowth occurs the grain has radius $R > R_0$. If n is the number of host grains per unit volume and ρ is the solid molar density of G, then the moles of G per unit rock volume, denoted G, is given by

$$G = \tfrac{4}{3}\pi n\rho\left[R^3 - R_0^3\right]. \tag{A.1}$$

The rate of growth of volume of a grain is taken to be proportional to the surface area $4\pi R^2$. Hence we write

$$\frac{\partial}{\partial t}\left[\frac{4}{3}\pi R^3\right] = 4\pi k' R^2[XF - Q], \tag{A.2}$$

where the last factor is based on a mass action growth kinetics. The rate coefficient k' is assumed constant. Combining (A.1, A.2) yields

$$\frac{\partial G}{\partial t} = k[G + g_0]^{2/3}[XF - Q], \tag{A.3}$$

where

$$k = 4\pi k'/\left(\tfrac{4}{3}\pi n\rho\right)^{2/3}, \tag{A.4}$$

$$g_0 = \tfrac{4}{3}\rho R_0^3. \tag{A.5}$$

To account for nucleation we replace g_0 by a factor g which is g_0 unless $G = 0$ and FX does not exceed a threshold value Q_n; in the latter case $g = 0$ so that no G growth starts if the nucleation threshold is not exceeded.

References

[1] P. Ortoleva and J. Ross, J. Chem. Phys. 60 (1974) 5090.
[2] P. Hanusse, P. Ortoleva and J. Ross, Adv. in Chem. Phys. (1978), 317 pp.
[3] D.G. Aronson and H.F. Weinberger, Lecture Notes in Math. 446 (1975).
[4] P. Fife, Bull. of AMS 84 (1978) 693.
[5] P. Ortoleva and S. Schmidt, "The variety and structure of chemical waves", in: Oscillations and Traveling Waves in Chemical Systems, R.J. Field and M. Burger, eds. (Wiley, New York, 1985) pp. 333–413.
[6] G. Nicolis and I. Prigogine, Self-Organization in Nonequilibrium Systems (Wiley, New York, 1977).
[7] H.C. Granger and C.G. Warren, Econ. Geol. 64 (1969) 160.
[8] W.E. Galloway and W.R. Kaiser, Bureau Economic Geology, Univ. of Texas, Rept. No. 100 (1980), 81 pages.
[9] R.M. Capuano, "Chemical mass transfer and solution flow in Wyoming roll-type uranium deposits: Master's Thesis, Univ. of Arizona (1977), 81 pages.
[10] A. Friedman, Partial Differential Equations of Parabolic Type (Prentice-Hall, Englewood Cliffs, NJ, 1964).
[11] J. Chadam and P. Ortoleva, "Moving interfaces and their stability: Application to chemical waves and solidification," in: Dynamics of Nonlinear Systems: Chemical Engineering Concepts and Reviews, vol. 2, V. Hlavacek, ed. (Gordon and Breach, New York, 1986) pp. 247–278.
[12] S. Schmidt and P. Ortoleva, J. Chem. Phys. 72 (1981) 2733; 74 (1981) 4488.
[13] G. Auchmuty, J. Chadam, E. Merino, P. Ortoleva and E. Ripley, "The stability and structure of propagating redox fronts," SIAM Journ. Appl. Math. in press.
[14] J. Chadam, D. Hoff, E. Merino, P. Ortoleva and A. Sen, "Reaction percolation instabilities," J. Appl. Math., submitted.
[15] W. Ostwald, Kolloid-Z 36 (1925) 380.
[16] S. Prager, J. Chem. Phys. 25 (1956) 279.
[17] R. Feeney, S. Schmidt, P. Strickholm, J. Chadam and P. Ortoleva, J. Chem. Phys. 78 (1983) 1293.
[18] P. Ortoleva, "The self-organization of Liesegang bands and other precipitate patterns", in: Chemical Instabilities: Applications in Chemistry, Engineering, Geology and Materials Science, G. Nicolis, and F. Baras, eds., NATO Advanced Science Series C, V. 120 (1984), pp. 289–297.
[19] R.E. Liesegang, Phot. Archiv. 21 (1896) 221.
[20] E. Hedges and J.E. Myers, The Problem of Physico-Chem-

ical Periodicity (Longmans-Green, New York, 1926).
[21] E. Merino, "Survey of geochemical self organization", in: Chemical Instabilities: Applications in Chemistry, Engineering, Geology, and Materials Science, G. Nicolis, and F. Baras, eds., NATO Adv. Sci. Series C, V. 120 (1984), pp. 305–328.
[22] P. Ortoleva, "Modeling nonlinear wave propagation and pattern formation at geological first order phase transitions", in: Chemical Instabilities: Applications in Chemistry, Engineering, and Materials Science, G. Nicolis and F. Baras, eds., NATO Adv. Sci. Series C, V. 120 (1984), pp. 329–340.